Acta Crystallographica Section D
Biological Crystallography
ISSN 1399-0047

Crystallographic study of FABP5 as an intracellular endocannabinoid transporter

Benoît Sanson,[a] Tao Wang,[a]‡ Jing Sun,[b] Liqun Wang,[b] Martin Kaczocha,[b] Iwao Ojima,[c,d] Dale Deutsch[b,d]* and Huilin Li[a,b,d]*

[a]Biosciences Department, Brookhaven National Laboratory, Upton, NY 11973-5000, USA, [b]Department of Biochemistry and Cell Biology, Stony Brook University, Stony Brook, NY 11794-5213, USA, [c]Department of Chemistry, Stony Brook University, Stony Brook, NY 1794-3400, USA, and [d]Institute of Chemical Biology and Drug Discovery, Stony Brook University, Stony Brook, NY 11794-3400, USA

‡ Current address: School of Chemical Biology and Biotechnology, Shenzhen Graduate School, Peking University, Shenzhen 518055, People's Republic of China.

Correspondence e-mail: dale.deutsch@stonybrook.edu, hli@bnl.gov

Received 10 May 2013
Accepted 30 September 2013

PDB references: mouse FABP5, 4azn; 4azo; complex with AEA, 4azp; complex with 2-AG, 4azq; human FABP5, complex with BMS-309403, 4azm; complex with AEA, 4azr

In addition to binding intracellular fatty acids, fatty-acid-binding proteins (FABPs) have recently been reported to also transport the endocannabinoids anandamide (AEA) and 2-arachidonoylglycerol (2-AG), arachidonic acid derivatives that function as neurotransmitters and mediate a diverse set of physiological and psychological processes. To understand how the endocannabinoids bind to FABPs, the crystal structures of FABP5 in complex with AEA, 2-AG and the inhibitor BMS-309403 were determined. These ligands are shown to interact primarily with the substrate-binding pocket *via* hydrophobic interactions as well as a common hydrogen bond to the Tyr131 residue. This work advances our understanding of FABP5–endocannabinoid interactions and may be useful for future efforts in the development of small-molecule inhibitors to raise endocannabinoid levels.

1. Introduction

Endocannabinoids are signaling lipids that activate cannabinoid receptors in the central nervous system and peripheral tissues (Howlett *et al.*, 2011). The best characterized endocannabinoids, anandamide (AEA) and 2-arachidonoylglycerol (2-AG), are ethanolamine and glycerol derivatives of arachidonic acid, respectively. In contrast to hydrophilic neurotransmitters, endocannabinoids are not stored in vesicles. Instead, the magnitude and duration of endocannabinoid signaling is regulated through 'on demand' biosynthesis and prompt catabolism. AEA is principally hydrolyzed by fatty-acid amide hydrolase (FAAH), while 2-AG is inactivated by monoacylglycerol lipase (MAGL), ABHD6 and ABHD12 (Cravatt *et al.*, 2001; Blankman *et al.*, 2007; Deutsch & Chin, 1993).

Owing to their limited solubility, endocannabinoids require carrier-assisted transport through the cellular cytoplasm. Recently, we identified fatty-acid-binding proteins (FABPs) as intracellular carriers that transport AEA from the plasma membrane to intracellular FAAH for hydrolysis (Kaczocha *et al.*, 2009). FABPs are small (~15 kDa) widely expressed intracellular lipid-binding proteins (Furuhashi & Hotamisligil, 2008) and bind a variety of lipophilic ligands including fatty acids, fatty-acid amides and xenobiotics (Velkov *et al.*, 2005; Chuang *et al.*, 2008; Kaczocha *et al.*, 2012).

It is well established that inhibition of FAAH or MAGL potentiates endocannabinoid-mediated antinociceptive and anti-inflammatory effects (Ahn *et al.*, 2009; Long *et al.*, 2009). Inhibition of intracellular endocannabinoid carriers such as FABPs may provide an alternative strategy to modulate endocannabinoid inactivation. We have previously shown that FABP knockdown or inhibition with the selective inhibitor

BMS-309403 (Sulsky *et al.*, 2007) reduces AEA inactivation in cells (Kaczocha *et al.*, 2009). FABP inhibitors augment endocannabinoid levels and produce beneficial anti-inflammatory and antinociceptive effects (Berger *et al.*, 2012). As such, the design of novel selective FABP inhibitors hinges upon understanding the bonding interactions between current-generation inhibitors and the FABP-binding pocket.

Ten isoforms of FABP have been identified in various tissues, with FABP4 mainly present in adipocytes and FABP5 in epidermis (Furuhashi & Hotamisligil, 2008). At the primary-sequence level, the conservation of FABP isoforms varies from low (∼15%) to very high (∼70%). The FABPs are conserved in three-dimensional structure: they form a ten-stranded β-barrel (Furuhashi & Hotamisligil, 2008; Hamilton, 2004). The β-barrel is comprised of two orthogonal five-stranded β-sheets: β-sheet 1 and β-sheet 2. One side of the β-barrel is capped by a helix–loop–helix motif and the other side by the amino-terminal peptide. Therefore, the structure is also referred to as a β-clamshell, with the two β-sheets as a pair of valves (Sacchettini *et al.*, 1989; Hodsdon & Cistola, 1997; Jenkins *et al.*, 2002; Richieri *et al.*, 1999). Endogenous fatty acids such as palmitic acid and oleic acid generally bind to FABPs in a similar manner, with their carboxylates binding to one or two conserved basic residues and their hydrocarbon chains nesting in the largely hydrophobic chambers (Furuhashi & Hotamisligil, 2008; Hohoff *et al.*, 1999). In this study, we determined the crystal structures of mouse and human FABP5 in complex with AEA or 2-AG and with the inhibitor BMS-309403. These two proteins are highly conserved, with 80% (108/135 residues) sequence identity.

2. Experimental procedures

2.1. Cloning, expression and purification of human and mouse FABP5

The FABP constructs were as described by Kaczocha *et al.* (2012) and the purification of the FABPs was based on a published procedure (Hohoff *et al.*, 1999). Briefly, both human and mouse FABP5 sequences were encoded into the pET-28a vector (Novagen) fused with an N-terminal 6×His tag. Proteins were expressed in *Escherichia coli* BL21(DE3) cells using the T7 expression system. Cells were grown in LB medium at 37°C with shaking at 250 rev min^{-1}. At an OD_{600} of ∼0.7, protein expression was induced by adding IPTG to a concentration of 0.4 m*M*. After 20 h incubation at 20°C, the cells were pelleted by centrifugation at 5000*g* at 4°C for 15 min and then resuspended in 30 ml ice-cold column buffer (250 m*M* NaCl, 20 m*M* Tris pH 8.5). These cells were lysed by sonication on ice, followed by 30 min centrifugation at 15 000*g* at 4°C. The supernatant was loaded onto an Ni–NTA column (Qiagen, Valencia, California, USA). After mixing the supernatant with Ni–NTA agarose at 4°C for 10 min, the column was washed with ten bed volumes of column buffer containing 20 m*M* imidazole. The protein was then eluted with column buffer containing 200 m*M* imidazole. The affinity-purified samples were concentrated on a Spin-X UF cartridge (Corning, England) and loaded onto a Sephacryl S-100 XK 16/70 column equilibrated with 1× PBS pH 8.5 using an ÄKTAprime plus system (GE Healthcare Life Sciences). The peak fractions were collected and delipidated by incubation with Lipidex-5000 (Sigma) at 37°C for 1 h with occasional mixing.

For preparations where the 6×His tag was removed, the affinity-purified proteins were incubated with thrombin (GE Healthcare Life Sciences) at 10 units per milligram of protein at 4°C overnight. The reaction was stopped by the addition of phenylmethylsulfonyl fluoride to a final concentration of 1 m*M*. The solution was loaded onto an Ni–NTA column and the unbound fractions containing the 6×His-tag-cleaved FABP5 was collected and then concentrated. The concentrated sample was subjected to the same gel-filtration chromatography and delipidation procedure as described above. All purified proteins were concentrated to approximately 10 mg ml^{-1} and then stored at −80°C.

2.2. Crystallization and structural solution

The frozen purified mouse FABP5 was thawed on ice. Crystals of the 6×His-tagged mouse FABP5 grew in 20% PEG 3350, 100 m*M* bis-tris pH 5.5. Crystals of the tag-cleaved mouse FABP5 grew in 50 m*M* sodium acetate pH 4.8, 5% MPD, 25% PEG 3350, 200 m*M* NaCl. Some crystals were soaked overnight in the mother liquor supplemented with 25% glycerol and saturated with AEA or 2-AG.

Frozen samples of the tag-free human FABP5 were thawed on ice and incubated with saturating concentrations of AEA or the inhibitor BMS-309403. The AEA–FABP5 complex was co-crystallized in 25% PEG 3350, 0.1 *M* HEPES pH 7.5. The inhibitor–FABP5 complex was co-crystallized in 1.32 *M* sodium citrate, 0.1 *M* HEPES pH 7.0. The crystals were cryoprotected in mother liquor containing 25 or 28% glycerol in the case of the complexes with AEA and the inhibitor, respectively.

X-ray diffraction data were collected on beamlines X25 and X29 at the National Synchrotron Light Source and were integrated and scaled using *XDS* (Kabsch, 2010). We set aside 5% of the reflections as the test set. The structures were solved by molecular replacement using PDB entry 1b56 (Hohoff *et al.*, 1999) as a search model. Structure refinement was performed using *REFMAC* (Murshudov *et al.*, 2011). TLS refinement was carried out as a final step, which generally improved the R_{work} and R_{free} factors by ∼1% (Painter & Merritt, 2006). We used two TLS groups per monomer in all models. Simulated-annealing OMIT maps, composite OMIT maps and $F_o - F_o$ difference maps were calculated using *CNS* (Brunger, 2007). Radiation damage was assessed using co-crystals of FABP5–BMS-309403 by calculating the $F_o - F_o$ difference maps between two successive data sets from the same region of a single crystal. All ligand molecules were built and their associated geometry files calculated using *PRODRG* (Schüttelkopf & van Aalten, 2004). The models were validated using *MolProbity* (Chen *et al.*, 2010). Figures were prepared using *PyMOL* (http://www.pymol.org). The

Table 1
Statistics of data collection and structure refinement.

Values in parentheses are for the last resolution shell.

	mFABP5 (His-tagged)	mFABP5	mFABP5	mFABP5	hFABP5	hFABP5
Data collection						
Ligand	—	—	AEA	2-AG	BMS	AEA
Space group	*C*2	$P6_422$	$P6_422$	$P6_422$	$P42_12$	$C222_1$
Unit-cell parameters						
a (Å)	97.29	79.32	79.71	79.48	104.57	66.12
b (Å)	64.97	82.32	83.15	82.70	58.61	115.15
c (Å)	60.10	82.32	83.15	82.70	58.61	108.35
$\alpha = \beta$ (°)	90	90	90	90	90	90
γ (°)	122.34	120	120	120	90	90
Oscillation (°)	1	1	1	1	1	1
Exposure (s)	1	2	1	1	1	3
Maximum resolution (Å)	2.50	2.33	2.10	2.00	2.75	2.95
Completeness (%)	93.7 (62.0)	99.2 (98.9)	99.4 (99.2)	99.6 (100)	99.9 (100)	99.9 (100)
R_{merge}† (%)	5.2 (21.6)	4.0 (45.5)	6.8 (48.1)	8.1 (51.5)	6.2 (60.1)	11.2 (57.8)
Multiplicity	7.4	10.6	11.4	11.4	12.4	6.5
$\langle I/\sigma(I)\rangle$	28.4 (8.2)	33.1 (4.0)	22.0 (5.3)	18.5 (4.9)	35.6 (4.7)	16.1 (3.2)
Refinement						
Resolution range (Å)	20–2.51	20–2.33	20–2.10	20–2.00	20–2.75	20–2.95
R_{cryst}‡ (%)	21.44	22.44	19.95	21.63	20.50	21.91
R_{free}‡ (%)	28.19	27.39	23.62	25.73	25.20	26.80
No. of protein atoms	2132	1060	1053	1079	2101	2108
No. of waters	82	27	84	68	44	32
No. of ligands	0	0	1	1	1	1
R.m.s.d., bond lengths (Å)	1.606	1.402	1.412	1.392	1.450	1.293
R.m.s.d., bond angles (°)	0.015	0.011	0.012	0.011	0.011	0.012
Average *B* factor (Å^2)	51.6	56.4	40.2	44.1	55.2	38.5
Ramachandran quality						
Favored (%)	95.9	99.2	99.2	98.5	97.4	95.9
Outliers (%)	0.0	0.0	0.0	0.0	0.4	0.0
TLS groups per chain	2	2	2	2	2	2
PDB code	4azn	4azo	4azp	4azq	4azm	4azr

† $R_{merge} = \sum_{hkl}\sum_i |I_i(hkl) - \langle I(hkl)\rangle|/\sum_{hkl}\sum_i I_i(hkl)$. ‡ $R = \sum_{hkl}||F_{obs}| - |F_{calc}||/\sum_{hkl}|F_{obs}|$ for both R_{cryst} and R_{free}. R_{cryst} is calculated from the working data set, whereas R_{free} is calculated from the test set (5% of the total reflections).

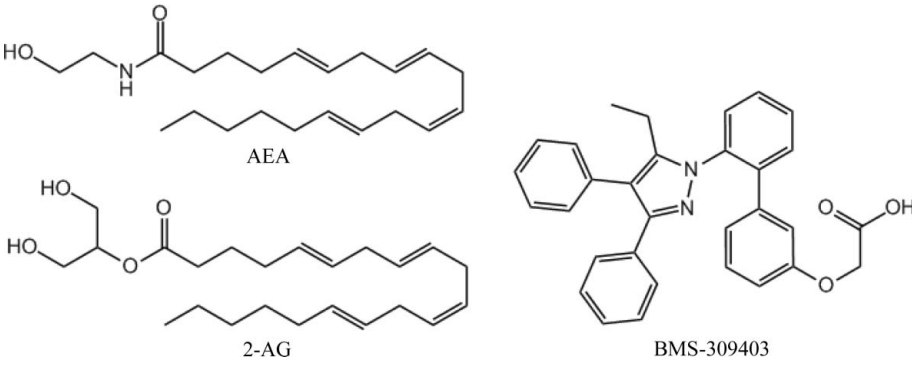

Figure 1
The chemical structures of AEA, 2-AG and the FABP inhibitor BMS-309403.

atomic coordinates and structure factors have been deposited in the PDB as entries 4azn, 4azo, 4azp, 4azq, 4azm and 4azr.

3. Results and discussion

3.1. Crystal structures of mouse FABP5 in complex with AEA

AEA is an arachidonic acid derivative containing four double bonds, with a chemical composition of $C_{22}H_{37}NO_2$ and a mass of 347 Da (Fig. 1). To determine by X-ray crystallography how AEA binds to FABP5, we overexpressed mouse FABP5 in *E. coli* and purified the protein by Ni^{2+}-affinity column chromatography *via* an engineered 6×His tag at the amino-terminus of the protein. We found that the His-tag mediated crystal contact by interaction with β-strand 4 of a neighboring protein molecule, potentially interfering with the FABP5 structure (Supplementary Fig. S1[1]; Table 1; PDB entry 4azn). In subsequent work, we removed the His tag by thrombin cleavage and then delipidated the purified FABP by treatment with Lipidex-5000 (see §2). The resulting protein was concentrated and stored at −80°C.

The delipidated mouse FABP5 was first crystallized in space group $P6_422$ and the apo FABP5 structure was solved at 2.33 Å resolution (Table 1; PDB entry 4azo). We then soaked the crystals in saturated solutions of AEA. The structure of the FABP5–AEA complex was solved at 2.1 Å resolution (Table 1; PDB entry 4azp; Fig. 2). The protein structures were essentially the same in the presence or absence of AEA. The presence of AEA in the substrate-soaked crystals was demonstrated by the elongated electron density inside the substrate-binding pocket of the $F_o - F_c$ electron-density map (Fig. 2*b*). The initial density for the ligand was rather weak and contained gaps. The AEA model was initially built into the $F_o - F_c$ map. We also calculated composite OMIT maps to confirm the placement of AEA.

In the crystal structure, the hydroxyl group of AEA forms a hydrogen bond to Tyr131 and a second, water-mediated, hydrogen bond to Arg129 (Fig. 2*c*). The long lipophilic chain of AEA forms a loop that nests in the largely hydrophobic substrate pocket, with the nearest residues being Tyr22, Leu26, Leu32, Ala36, Pro41, Val60, Ala78 and Val118, mostly from the N-terminal region of the transporter. Interestingly, a recent molecular-dynamics simulation of AEA complexed with FABP7 predicted a similar mode of binding (Howlett *et al.*, 2011). AEA was shown to bind to FABP5 with an affinity of ∼1.3 μ*M*, approximately tenfold lower than its parent fatty acid arachidonic acid (Kaczocha *et al.*, 2012). Consistent with

[1] Supporting information has been deposited in the IUCr electronic archive (Reference: XB5074).

this lower binding affinity, we found that the electron densities at both ends of AEA are weak. We suggest that the binding at the terminal regions of the AEA molecule in FABP5 may be less specific and may have multiple conformations; therefore, the model as built may represent an average of these conformations.

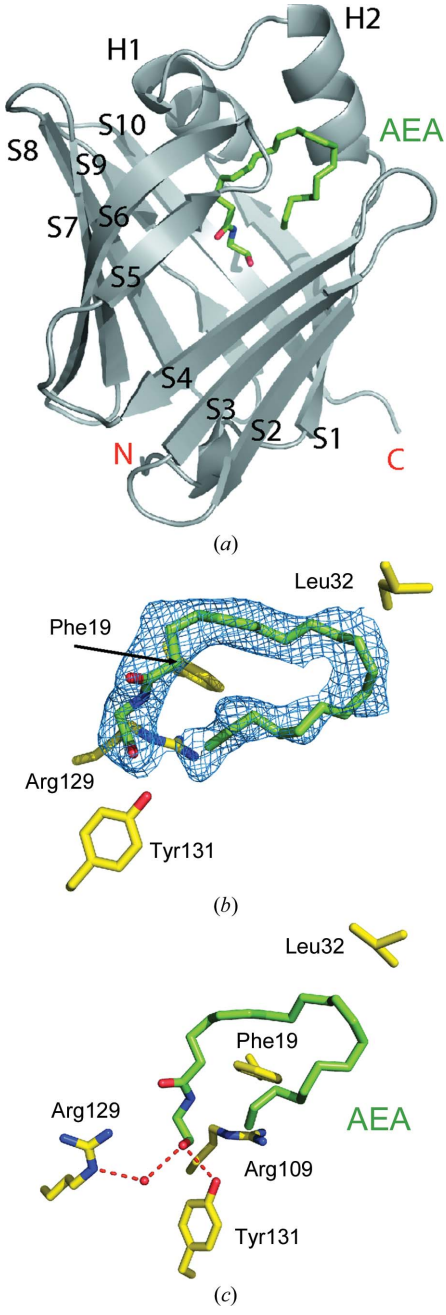

Figure 2
Interactions between AEA and mouse FABP5. (*a*) Cartoon view of the FABP5–AEA complex crystal structure. The secondary-structural elements, α-helices H1 and H2 and β-strands S1–S10, are labeled. The red letters 'N' and 'C' denote the amino- and carboxyl-termini of the protein, respectively. The bound AEA is shown as green sticks. (*b*) Electron density of AEA in the binding pocket of FABP5. The simulated OMIT map is contoured at the 2.5σ threshold and is shown as a blue mesh. (*c*) Detailed interactions between AEA (green sticks) and FABP5 (contacting residues shown as yellow sticks).

Because AEA is longer than the most common endogenous ligand, palmitic acid, we examined whether AEA binding causes structural changes in FABP5 compared with that of palmitic acid (Supplementary Fig. S2; PDB entries 4azp and 1b56; Hohoff *et al.*, 1999). We found that AEA binds to FABP5 in a manner similar to that of palmitic acid. However, the extra length of the AEA hydrocarbon tail has pushed the surrounding H1–H2 motif and the S3–S4 loop outwards by 1.5–2 Å. Since the H1–H2 cap and S3–S4 loops are generally considered to line the substrate entrance, our observed movement of these structural components by AEA is consistent with such a substrate-entrance model.

3.2. Crystal structure of mouse FABP5 in complex with 2-AG

2-AG was the second endocannabinoid to be discovered following AEA. 2-AG is a glycerol derivative of arachidonic acid (Fig. 1). The structure of 2-AG complexed with mouse FABP5 was solved at 2.0 Å resolution using essentially the

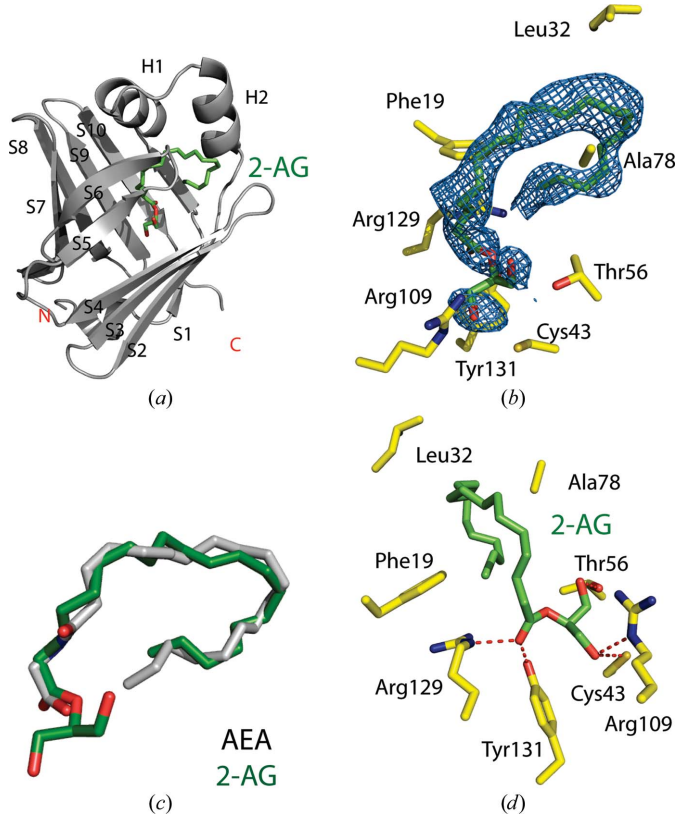

Figure 3
Crystal structure of mouse FABP5 in complex with 2-AG. (*a*) Cartoon view of the structure. The secondary-structural elements, α-helices H1 and H2 and β-strands S1–S10, are labeled. The bound 2-AG is shown as green sticks. The red letters 'N' and 'C' denote the amino- and carboxyl-termini of the protein, respectively. (*b*) Electron density of 2-AG in the binding pocket of the FABP5–2-AG complex. The simulated OMIT map is contoured at the 2.5σ threshold and is displayed as a blue mesh. (*c*) Superposition of 2-AG with AEA in mFABP5. The two 2-AG hydroxyl groups insert deeper into the substrate chamber. (*d*) Detailed interactions between 2-AG and FABP5. Hydrogen bonds are shown as red dashes. Note that the viewing direction of (*d*) is ~90° rotated from that in (*b*) to provide a different perspective. The FABP5 residues close to or in contact with 2-AG are shown as yellow sticks.

same procedure as described above (Fig. 3; Table 1; PDB entry 4azq). The electron density of 2-AG is stronger than that of AEA except at the non-alkyl end of 2-AG, where it is slightly weaker (Figs. 3*b* and 2*b*). Compared with AEA, the hydrophilic head group of 2-AG inserts deeper into the substrate pocket (Fig. 3*c*). In the crystal structure, the lowered head position of 2-AG enables it to form five hydrogen bonds to the transporter (Fig. 3*d*), namely between the carbonyl O atom of 2-AG and Arg129, between the carbonyl O atom of 2-AG and Tyr131, between Arg109 and one hydroxyl of 2-AG, which also makes a hydrogen bond to Cys43, and between the second hydroxyl group and Thr56. The looped lipophilic fragment of 2-AG is within 4 Å distance of FABP5 residues Phe19, Ala36, Val60, Ala78, Ile107 and Val118.

The two endocannabinoids have similar chemical structures (Fig. 1). Both are sparsely branched alkyl chains with nearly identical lengths: the alkyl chain of AEA has 22 C atoms and that of 2-AG has 23 C atoms. By comparing their binding modes to FABP5, we note that Tyr131 and Arg129 of FABP5 make hydrogen bonds to the polar ends of both ligands and that essentially the same residues of the transporter are involved in hydrophobic contacts with the lipophilic arachidonyl chain (Figs. 2*c* and 3*d*). However, AEA forms fewer hydrogen bonds than 2-AG, but AEA is in tighter hydrophobic contact with FABP5 than 2-AG. Their binding modes are consistent with their similar binding affinity to FABP5, which is 1.26 ± 0.18 µ*M* for AEA and 1.45 ± 0.21 µ*M* for 2-AG (Kaczocha *et al.*, 2012). The experimental electron densities for these endocannabinoids are weak at the ends and are partially broken (Figs. 2*b* and 3*b*), suggesting that both AEA and 2-AG may adopt multiple conformations at their respective termini in FABP5.

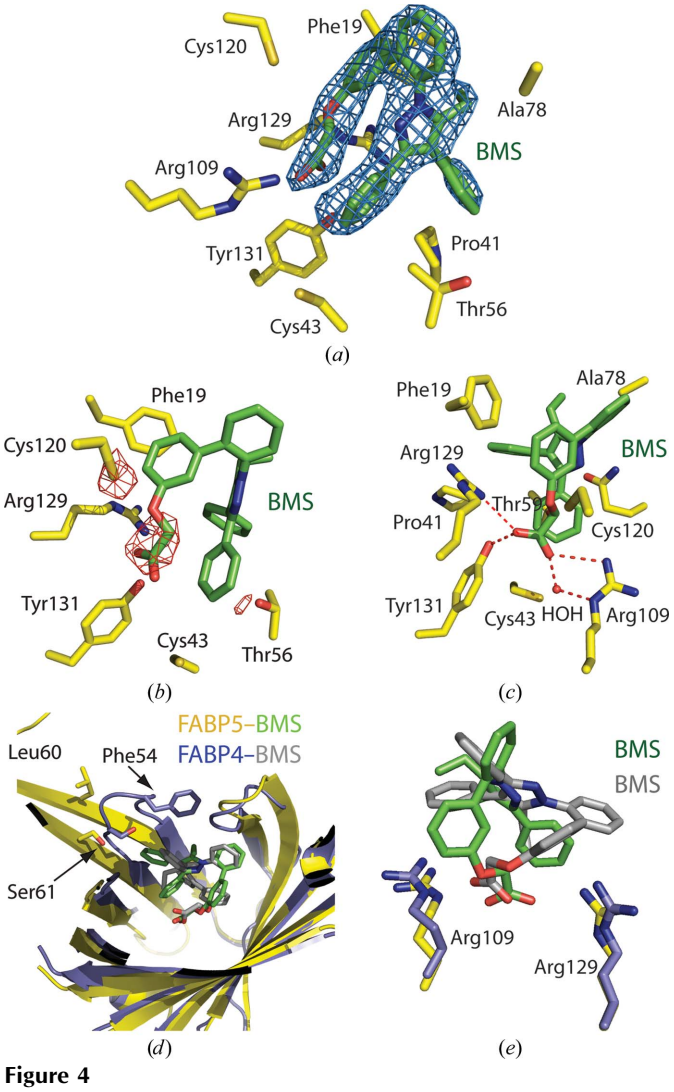

Figure 4
The binding mode of BMS-309403 in human FABP5. (*a*) The simulated-annealing $F_o - F_c$ OMIT map calculated around the inhibitor is contoured at the 3σ level and is displayed as a blue mesh. (*b*) An $F_o - F_c$ difference density map calculated from two consecutive data sets collected from the same region of a single crystal. The map is contoured at the −3σ level and is shown as a red mesh. The loss of electrons at the carboxylic acid moiety of BMS-309403 and, to a lesser extent, at the S atom of Cys120 is caused by radiation damage. (*c*) The hydrogen-bonding network that stabilizes the inhibitor in the FABP5 substrate pocket. The hydrogen bonds are shown as red dashes. One water molecule is shown as a red ball. (*d*) Superposition of BMS-309403 in complex with FABP5 (in yellow) with the same inhibitor complexed to FABP4 (PDB entry 2nnq; blue; Sulsky *et al.*, 2007). Several residues surrounding the inhibitors are shown as sticks. (*e*) Enlarged view of the BMS-309403 structure bound to FABP5 (green) superimposed on the inhibitor bound to FABP4 (gray). BMS-309403 forms hydrogen bonds to two conserved arginine residues in both FABP4 (blue) and FABP5 (yellow). For clarity, hydrogen bonds are not shown.

3.3. Crystal structure of human FABP5 in complex with BMS-309403

BMS-309403 is a biphenyl azole that was initially developed as a high-affinity inhibitor of the adipocyte FABP4 (2 n*M*; Fig. 1) in an effort to develop anti-obesity drugs (Sulsky *et al.*, 2007). The crystal structure of the inhibitor in complex with FABP4 has previously been reported (Sulsky *et al.*, 2007). We found that the compound also inhibits human FABP5, although with a lower affinity of 890 n*M* (Kaczocha *et al.*, 2012). We have now determined the crystal structure of this inhibitor in complex with human FABP5 (Table 1; PDB entry 4azm), with the expectation that the binding mode would yield clues about how to improve the potency of the compound towards FABP5. Interestingly, the FABP5–inhibitor complex crystallized as a domain-swapped dimer (described further below). An $F_o - F_c$ map calculated before ligand modeling revealed a clear positive electron density in the substrate pocket. Inspection of the $F_o - F_c$ map showed that the electron density for one monophenyl ring is weak, probably as a result of rotational freedom (Fig. 4*a*). BMS-309403 contains a terminal carboxylate that, like cysteine, is known to be sensitive to radiation damage (Weik *et al.*, 2000; Garman & Weik, 2011). We collected two consecutive data sets from the same region of a single crystal and calculated an $F_o - F_c$ difference map. Displayed at a −3σ level, the difference map shows two negative electron-density peaks in the regions of the inhibitor carboxylate and Cys120, respectively (Fig. 4*b*), clearly indicating a loss of electrons owing to X-ray-induced oxidation of these chemical groups. This experiment confirms our modeling of the BMS-309403 inhibitor.

The binding modes of the inhibitor in the two monomers of the FABP5 dimer are very similar except that the inhibitor electron density is stronger in one monomer than in the other. This is reflected in their respective average *B* factors (55.9 and 70.2 Å^2, respectively). In the crystal structure, one carboxyl O atom of the inhibitor forms a hydrogen bond to Arg129 of the transporter and another hydrogen bond to Tyr131 (Fig. 4*c*). The other carboxyl O atom makes one direct and one water-mediated hydrogen bond to Arg109. Several hydrophobic contacts contribute to the binding; these include residues Tyr22, Leu26, Ala39, Pro41, Ile54 and Ala78 that are within 4 Å of the inhibitor. Phe19 appears to be particularly important because its side chain is even closer at only ∼3.0 Å away from the distal phenyl ring as well as from the ethyl moiety of the inhibitor. The central pyrazole ring and the oxyacetate group are the best defined moieties of the ligand. Indeed, the oxyacetate group is involved in hydrogen bonding between the inhibitor and the protein. The inhibitor forms a total of four hydrogen bonds to Tyr131, Arg109 and Arg129.

The primary sequences of human FABP4 and FABP5 are ∼55% identical and ∼72% homologous and share essentially the same structure. We superimposed the structures of the respective proteins both complexed with the same inhibitor BMS-309403 (Figs. 4*d* and 4*e*). We found that the four freely rotatable benzene rings of the inhibitor are in different conformations, apparently exploring the local landscapes of the two proteins. In FABP4, the ethyl group of the inhibitor is in van der Waals interaction with Ser53. This feature was noted previously as a key factor in the high-affinity binding (Sulsky *et al.*, 2007). In the domain-swapped FABP5, the ethyl group is next to but makes no direct interaction with Gly36. We suggest that this binding difference may contribute to the lowered affinity of the inhibitor for FABP5. Nevertheless, the inhibitor shares binding features in both structures. Firstly, the oxyacetate moiety of the inhibitor forms hydrogen bonds to the three same residues in both structures: Arg109 (106 in FABP4 residue numbering), Arg129 (126) and Tyr131 (128). Secondly, hydrophobic interactions dominate the binding mode in both structures.

3.4. Ligand-bound human FABP5 dimerizes *via* a domain-swapping mechanism

The human FABP5 structure was previously solved as a monomer either in its apo form or bound to exogenous lipid by NMR or X-ray crystallography (Gutiérrez-González *et al.*, 2002; Hohoff *et al.*, 1999). However, human FABP5 forms a domain-swapped dimer when complexed with BMS-309403 (Fig. 5; PDB entry 4azm). The crystals of the human FABP5–inhibitor complex belonged to space group $P42_12$.

To examine whether the inhibitor was the cause of the observed domain swapping, we also solved the crystal struc-

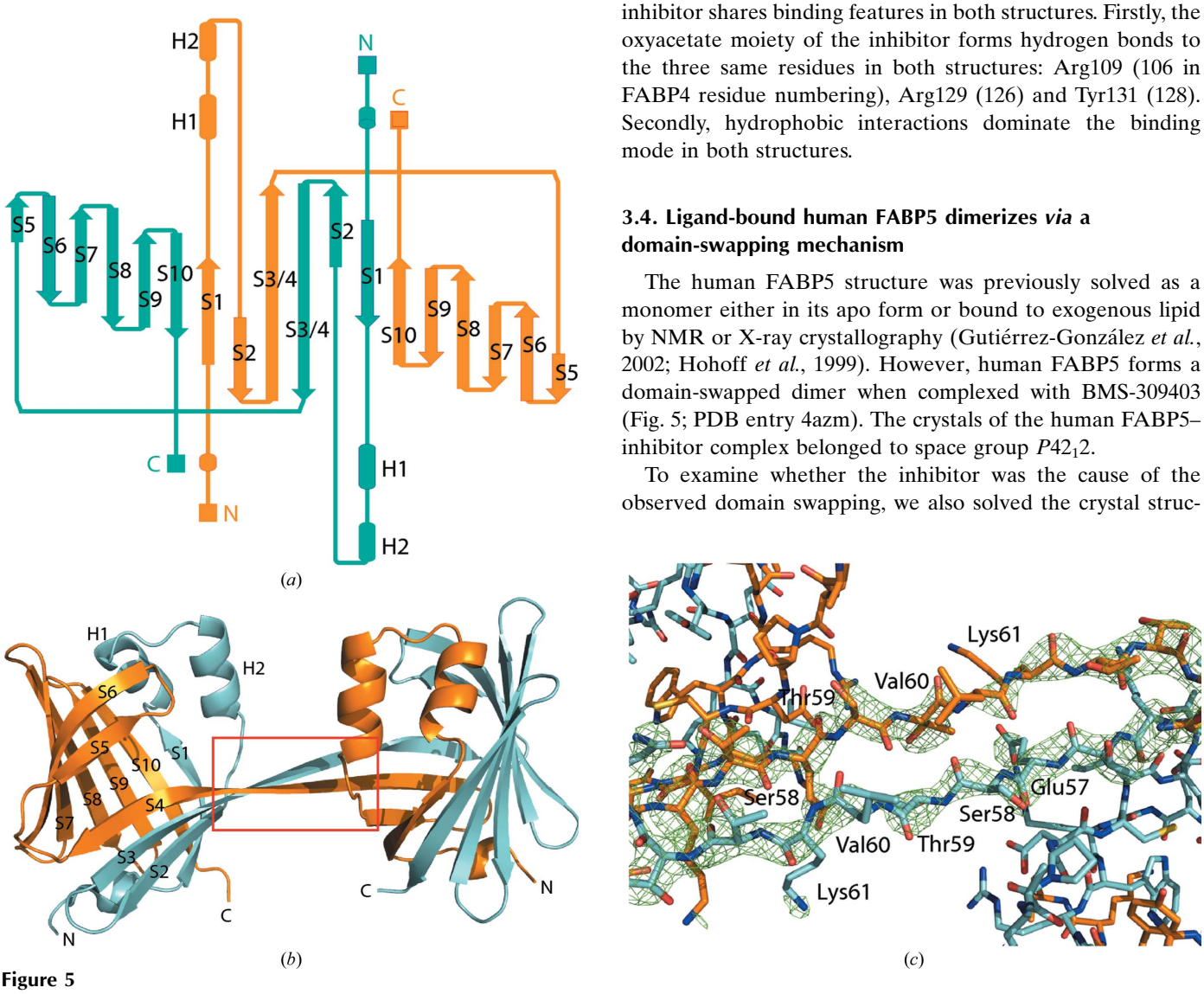

Figure 5
Human FABP5 crystallized as a domain-swapped dimer. (*a*) Topology diagram of the crystallographic domain-swapped dimer. The diagram was prepared in *Pro-origami* (Stivala *et al.*, 2011). (*b*) Overview of the dimeric FABP5 crystal structure. The secondary structure is shown as a cartoon view. The two FABP5 molecules are displayed in gold and cyan, respectively. (*c*) Close-up view of the induced β-strands extending between the two monomers in the domain-swapped FABP5 and the associated $F_o - F_c$ electron-density map. The map is contoured at the 3σ level and is shown as a green mesh. The region shown corresponds to the region in the red box in (*b*).

ture of human FABP5 in complex with AEA (Table 1; PDB entry 4azr). The human FABP5–AEA complex crystallized in a different space group, $C222_1$. We found that the human FABP5–AEA complex in the new crystal form is also a domain-swapped dimer, essentially the same as the dimer seen in the presence of BMS-309403 (Fig. 6). However, the binding mode of AEA in the domain-swapped human FABP5 dimer is modified compared with that in the monomeric mouse FABP5. Domain swapping of FABP5 makes the portal region more open (Fig. 6*a*), enabling the AEA to penetrate deeper into the substrate pocket (Fig. 6*b*) and resulting in an altered hydrogen-bonding interaction at the AEA head region (Fig. 6*c*). Because of the lower position of AEA, the hydroxyl group at the tip can no longer form a hydrogen bond to Tyr131. Instead, the hydrophilic AEA head region rotates by ∼180° compared with the structure in monomeric mFABP5, such that the hydroxyl now forms a hydrogen bond to Arg109. The lowered AEA orients its carbonyl group towards Tyr131 and forms a hydrogen bond to the hydroxyl of Tyr131.

In the FABP5 dimer structures, the N-terminal half of the first molecule (residues 1–59) forms a complete β-barrel with the C-terminal half of the second molecule (residues 60–134). In so doing, the loop (Glu57–Thr62) connecting the S3 and S4 β-strands in the monomeric structure is converted into a β-strand, and together with S3 and S4 forms an unusually long β-strand that connects the two domain-swapped monomers (Figs. 5*a* and 5*b*). The electron density in the connecting loop region between the S3 and S4 β-strands was impossible to model without swapping the N- and C-terminal subdomains of each monomer. Furthermore, a stretch of difference electron density appears if residues 57–62 from both chains are omitted during model building, clearly indicating the continuity of the β-strands across the two copies of the protein (Fig. 5*c*).

In the size-exclusion chromatography profile, the bacterially expressed and delipidated human FABP5 existed predominantly as a monomer and a dimer, with a smaller amount being in a higher oligomer state, possibly a tetramer (Supplementary Fig. S1). The presence or absence of substrates or inhibitors does not appear to affect the equilibrium between monomers and dimers. Fractions from the monomer peak, when subjected to another round of gel filtration, showed the coexistence of monomers and dimers. A similar gel-filtration profile was also observed for the purified and delipidated mouse FABP5 (Supplementary Fig. 1). This observation suggests that the quaternary structure of FABP5 in solution may be in a dynamic equilibrium between monomers and dimers.

Domain swapping is a recognized mechanism of protein

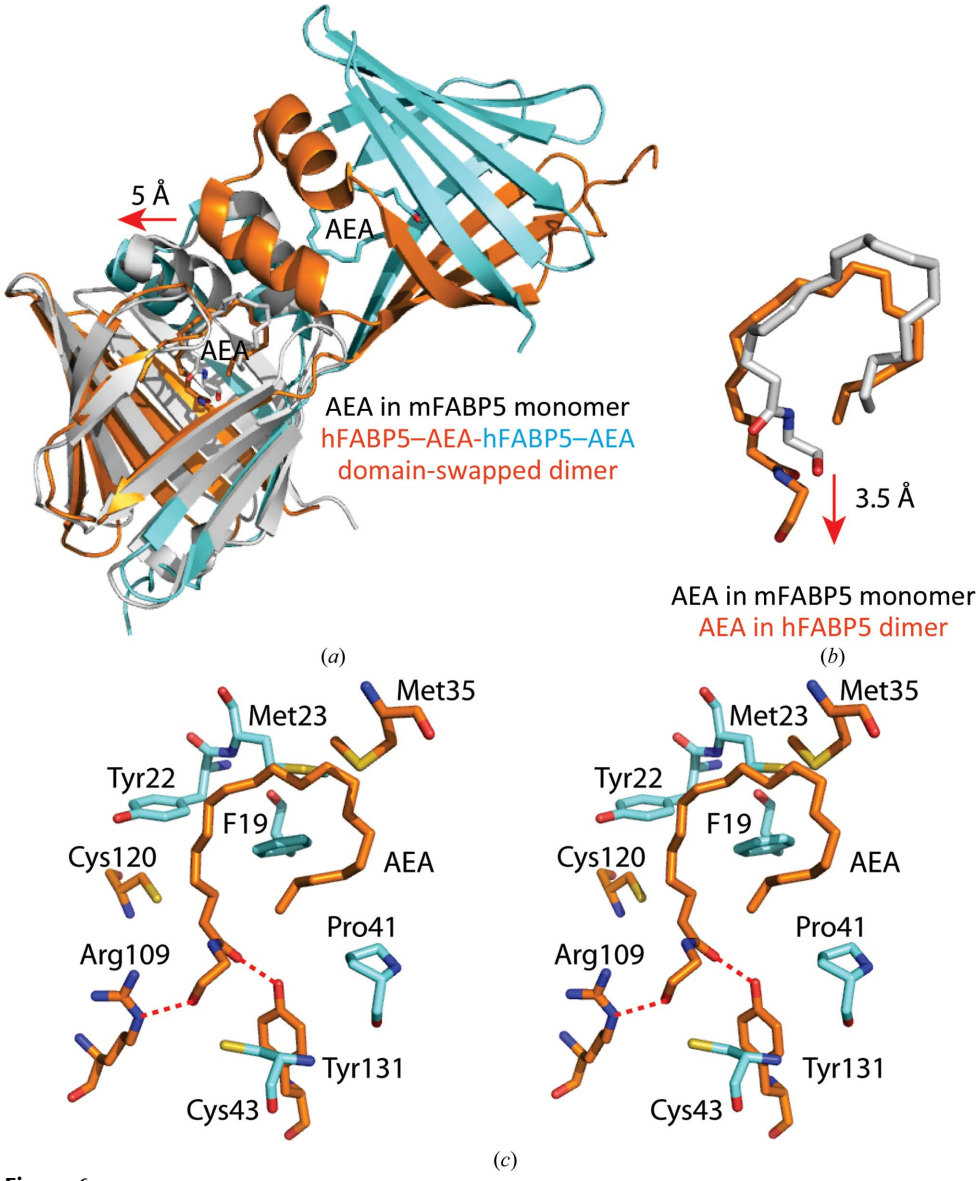

Figure 6
The AEA binding mode in domain-swapped human FABP5. (*a*) Superposition of hFABP5–AEA with mFABP5–AEA. The H1–H2 cap in hFABP5 (cyan) moves left by >5 Å compared with that in the monomer (gray), significantly opening up the portal region. (*b*) The AEA in the domain-swapped hFABP5 (orange) enters 3.5 Å deeper into the substrate chamber compared with that in the mFABP5 monomer (gray). (*c*) Stereoview of the interaction of AEA with hFABP5. The hydrocarbon chain of AEA is surrounded by Met35 and Cys120 of one FABP5 (orange) and by Phe19, Tyr22, Met23 and Pro41 of the other FABP5 (cyan). The AEA hydroxyl forms a hydrogen bond to Arg109 as shown by the dashed red line (2.7 Å). The AEA carbonyl forms a hydrogen bond to Tyr131 (2.4 Å).

oligomerization (Bennett *et al.*, 1995). The observed domain exchange in human FABP5 requires the transient breakage of several hydrogen bonds between S3 and S4 on one side and subsequently between S1 and S10 on the opposite side of the β-clamshell of the monomeric (unswapped) FABP5. The domain-swapped dimer may gain enthalpy because five additional hydrogen bonds form as the S3–S4 loop in the monomer structure is converted to the β-sheet configuration in the domain-swapped structure (Fig. 5*c*). However, the enthalpy gain is likely to be counterbalanced by a loss of entropy in the solvent-exposed monomeric S3–S4 loop region. As a result, the energy barrier associated with domain swapping in human FABP5 may be low enough to be within the reach of thermodynamic fluctuation (Bennett *et al.*, 1995). Domain swapping in human FABP5 may suggest that the protein structure is partially flexible and perhaps exhibits conformational dynamics.

It is thought that the lipophilic ligands enter and exit the deep and largely enclosed substrate cavity *via* the 'portal' region largely comprised of the capping helices H1 and H2 (Richieri *et al.*, 1999; Sacchettini *et al.*, 1989; Zhang *et al.*, 1997; Jenkins *et al.*, 2002; Chen *et al.*, 1998). Our observation of the outwards movement of the portal region of FABP5 bound to AEA compared with palmitic acid is indeed in agreement with such a model (Supplementary Fig. 2). However, the portal region alone may not be sufficient for admitting or releasing the large and hydrophobic substrates. For example, in the absence of steering forces the substrate failed to enter the binding pocket of FABP in a molecular-dynamics simulation (Friedman *et al.*, 2006). In a steered molecular-dynamics simulation in which the substrate was forced into the FABP pocket, it was found that the structure in the β-barrel region underwent significant changes (Tsfadia *et al.*, 2007). Therefore, the potential β-strand dynamics in human FABP5 may function in concert with the recognized portal region to facilitate substrate binding. Such a possibility merits further investigation. However, engineering a disulfide bond into FABP5 may be complicated by the presence of numerous cysteine residues (six) in both the human and the mouse proteins.

4. Conclusions

Understanding endocannabinoid transport and signaling is important for the development of small molecules that may serve as potential analgesics. Our crystallographic studies of FABP5 in complex with AEA and 2-AG provide structural evidence for our previous cell-based conclusion that endocannabinoids are transported intracellularly by FABP5. All three ligands described in this report, the ligands AEA and 2-AG and the inhibitor BMS-309403, bind to FABP5 *via* similar interactions that involve hydrogen bonding of their polar regions mainly to Tyr131 and Arg129 of the transporter and hydrophobic interactions of their lipophilic fragments with the side chains lining the substrate pocket of FABP5. The carrier substrate pocket contains multiple hydrophobic residues that appear to be sufficiently flexible to accommodate a variety of fatty-acid-like molecules. While mouse FABP5 was found only in the monomeric form, human FABP5 can exist as a monomer as well as a domain-swapped dimer, suggesting a higher degree of structural dynamics in the human protein. Such dynamics in human FABP5 presents a challenge as well as an opportunity for the development of the specific inhibitors.

This work was partially supported by an SBU/BNL Seed Grant from the Provost and by the Targeted Research Opportunity Fusion Award from the Medical School at Stony Brook University. DGD was supported by NIH DA016419 and DA026953. MK was supported by NIH DA032232. Diffraction data for this study were collected on beamlines X25 and X29 of the National Synchrotron Light Source. Financial support comes principally from the Offices of Biological and Environmental Research and of Basic Energy Sciences of the US Department of Energy and from the National Center for Research Resources (P41RR012408) and the National Institute of General Medical Sciences (P41GM103473) of the National Institutes of Health.

References

Ahn, K. *et al.* (2009). *Chem. Biol.* **16**, 411–420.
Bennett, M. J., Schlunegger, M. P. & Eisenberg, D. (1995). *Protein Sci.* **4**, 2455–2468.
Berger, W. T., Ralph, B. P., Kaczocha, M., Sun, J., Balius, T. E., Rizzo, R. C., Haj-Dahmane, S., Ojima, I. & Deutsch, D. G. (2012). *PLoS One*, **7**, e50968.
Blankman, J. L., Simon, G. M. & Cravatt, B. F. (2007). *Chem. Biol.* **14**, 1347–1356.
Brunger, A. T. (2007). *Nature Protoc.* **2**, 2728–2733.
Chen, V. B., Arendall, W. B., Headd, J. J., Keedy, D. A., Immormino, R. M., Kapral, G. J., Murray, L. W., Richardson, J. S. & Richardson, D. C. (2010). *Acta Cryst.* D**66**, 12–21.
Chen, X., Tordova, M., Gilliland, G. L., Wang, L., Li, Y., Yan, H. & Ji, X. (1998). *J. Mol. Biol.* **278**, 641–653.
Chuang, S., Velkov, T., Horne, J., Porter, C. J. & Scanlon, M. J. (2008). *J. Med. Chem.* **51**, 3755–3764.
Cravatt, B. F., Demarest, K., Patricelli, M. P., Bracey, M. H., Giang, D. K., Martin, B. R. & Lichtman, A. H. (2001). *Proc. Natl Acad. Sci. USA*, **98**, 9371–9376.
Deutsch, D. G. & Chin, S. A. (1993). *Biochem. Pharmacol.* **46**, 791–796.
Friedman, R., Nachliel, E. & Gutman, M. (2006). *Biophys. J.* **90**, 1535–1545.
Furuhashi, M. & Hotamisligil, G. S. (2008). *Nature Rev. Drug Discov.* **7**, 489–503.
Garman, E. F. & Weik, M. (2011). *J. Synchrotron Rad.* **18**, 313–317.
Gutiérrez-González, L. H., Ludwig, C., Hohoff, C., Rademacher, M., Hanhoff, T., Rüterjans, H., Spener, F. & Lücke, C. (2002). *Biochem. J.* **364**, 725–737.
Hamilton, J. A. (2004). *Prog. Lipid Res.* **43**, 177–199.
Hodsdon, M. E. & Cistola, D. P. (1997). *Biochemistry*, **36**, 2278–2290.
Hohoff, C., Börchers, T., Rüstow, B., Spener, F. & van Tilbeurgh, H. (1999). *Biochemistry*, **38**, 12229–12239.
Howlett, A. C., Reggio, P. H., Childers, S. R., Hampson, R. E., Ulloa, N. M. & Deutsch, D. G. (2011). *Br. J. Pharmacol.* **163**, 1329–1343.
Jenkins, A. E., Hockenberry, J. A., Nguyen, T. & Bernlohr, D. A. (2002). *Biochemistry*, **41**, 2022–2027.
Kabsch, W. (2010). *Acta Cryst.* D**66**, 133–144.
Kaczocha, M., Glaser, S. T. & Deutsch, D. G. (2009). *Proc. Natl Acad. Sci. USA*, **106**, 6375–6380.
Kaczocha, M., Vivieca, S., Sun, J., Glaser, S. T. & Deutsch, D. G. (2012). *J. Biol. Chem.* **287**, 3415–3424.

Long, J. Z., Li, W., Booker, L., Burston, J. J., Kinsey, S. G., Schlosburg, J. E., Pavón, F. J., Serrano, A. M., Selley, D. E., Parsons, L. H., Lichtman, A. H. & Cravatt, B. F. (2009). *Nature Chem. Biol.* **5**, 37–44.

Murshudov, G. N., Skubák, P., Lebedev, A. A., Pannu, N. S., Steiner, R. A., Nicholls, R. A., Winn, M. D., Long, F. & Vagin, A. A. (2011). *Acta Cryst.* D**67**, 355–367.

Painter, J. & Merritt, E. A. (2006). *Acta Cryst.* D**62**, 439–450.

Richieri, G. V., Low, P. J., Ogata, R. T. & Kleinfeld, A. M. (1999). *Biochemistry*, **38**, 5888–5895.

Sacchettini, J. C., Gordon, J. I. & Banaszak, L. J. (1989). *J. Mol. Biol.* **208**, 327–339.

Schüttelkopf, A. W. & van Aalten, D. M. F. (2004). *Acta Cryst.* D**60**, 1355–1363.

Stivala, A., Wybrow, M., Wirth, A., Whisstock, J. C. & Stuckey, P. J. (2011). *Bioinformatics*, **27**, 3315–3316.

Sulsky, R. *et al.* (2007). *Bioorg. Med. Chem. Lett.* **17**, 3511–3515.

Tsfadia, Y., Friedman, R., Kadmon, J., Selzer, A., Nachliel, E. & Gutman, M. (2007). *FEBS Lett.* **581**, 1243–1247.

Velkov, T., Chuang, S., Wielens, J., Sakellaris, H., Charman, W. N., Porter, C. J. & Scanlon, M. J. (2005). *J. Biol. Chem.* **280**, 17769–17776.

Weik, M., Ravelli, R. B. G., Kryger, G., McSweeney, S., Raves, M. L., Harel, M., Gros, P., Silman, I., Kroon, J. & Sussman, J. L. (2000). *Proc. Natl Acad. Sci. USA*, **97**, 623–628.

Zhang, F., Lücke, C., Baier, L. J., Sacchettini, J. C. & Hamilton, J. A. (1997). *J. Biomol. NMR*, **9**, 213–228.